NDT&E International 146 (2024) 103144

Contents lists available at ScienceDirect

NDT and E International

journal homepage: www.elsevier.com/locate/ndteint

Research Paper

Simultaneous Multi-frequency lock-in Thermography: A new flexible and effective Active Thermography scheme

Stefano Laureti [a,*], Paolo Bison [b], Giovanni Ferrarini [b], Rocco Zito [a], Marco Ricci [a]

[a] *Università della Calabria, Via Pietro Bucci 42, Arcavacata di Rende (CS), 87036, Italy*
[b] *CNR-ITC, Corso Stati Uniti 4, Padova, 35127, Italy*

ARTICLE INFO

Keywords:
Active thermography
Multi-frequency thermography
Multi-frequency lock-in
Multi-frequency signal
Carbon fiber reinforced plastic
SNR

ABSTRACT

A new active thermography scheme is here introduced, referred as "‘Multi-Frequency Thermography"', which uses an optimized multi-tone signal for simultaneously implementing lock-in analysis on a discrete and arbitrary set of linearly spaced frequencies. Such a signal, which modulates the intensity of the heating source here being a LED system in the visible range, results from the non-trivial summation of a desired number of odd and even harmonics of a fundamental tone, each of them having a specific initial phase value but equal amplitude, so as to deliver the same energy amount for all the chosen frequencies. In this way, a discrete set of thermal waves having different diffusion lengths are simultaneously excited within the inspected sample to probe different depths into it. With respect to standard lock-in thermography, it is demonstrated that the proposed approach can extract amplitude and phase features for all the excited frequencies from a single measurement, which lasts as long as a lock-in implemented at the fundamental tone. Both quantitative and qualitative comparisons with standard lock-in thermography are here reported, showing an excellent agreement. Hence, this new active thermography scheme can provide several advantages in practical implementations of thermography nondestructive evaluation.

1. Introduction

Active thermography (AT) is widely employed for the non-destructive evaluation (NDE) of a plethora of items and components [1], ranging from composites [2], to historical paintings [3] and food products [4], to mention some. In AT a heating stimuli is used to break the thermal equilibrium of the tested sample, so that abnormal temperature rises/decays of the specimen' surface can be imaged by means of a thermal camera. These areas are often related to defects/anomalies buried at a depth within the tested sample, thus it is crucial to enhance their thermal contrast with respect to the surrounding areas.

Despite the huge efforts on developing powerful post-processing algorithms for both interpreting quantitatively the acquired thermograms and maximizing the signal-to-noise ratio (SNR)/probability of detection of the defected areas [5,6], the heating stimuli is still deployed according to a few modulation strategies, see the taxonomy depicted in Fig. 1. In pulse thermography (PT), the heating source is turned on for a few milliseconds — the heating stimulus is a good approximation of the Dirac delta function $\delta(t)$ — provoking a sudden rise of the temperature of the targeted surface. The heat then diffuses within the sample, and potential anomalies are detected as areas having different temperatures/emissivity from the surrounding. Given the impulsive nature of the heating stimuli, i.e. the frequency spectrum of $\delta(t)$ can be considered flat within an extended yet limited bandwidth, the PT is an effective AT scheme when aiming at maximizing the number of information that can be inferred from a *single* test — the recorded thermograms can be used to gather extended knowledge about the anomalies, e.g., their sizes, compositions, and depths within the sample [7]. However, the SNR of the acquired thermograms is related to the deployed heat (usually limited by the available flash-lamp energy within $10^0 - 10^1$ kJ), so that subtle anomalies, or anomalies at relatively-large depth might not be detected faithfully.

Conversely, the thermal signature corresponding to a depth within the sample is maximized when modulating the heating/cooling stimuli at a specific frequency, using a single-frequency sinusoidal function of the time as the modulating waveform. This approach is referred to as Lock-in (LI) thermography [8,9]. However, in LI *multiple* tests are needed at a set of modulation frequencies values to excite a range of depths within the sample evenly, i.e. to onset a range of "‘thermal

* Corresponding author.
E-mail addresses: stefano.laureti@unical.it (S. Laureti), bison@itc.cnr.it (P. Bison), ferrarini@itc.cnr.it (G. Ferrarini), rocco.zito@dimes.unical.it (R. Zito), marco.ricci@dimes.unical.it (M. Ricci).

https://doi.org/10.1016/j.ndteint.2024.103144
Received 7 October 2023; Received in revised form 15 April 2024; Accepted 24 May 2024
Available online 1 June 2024

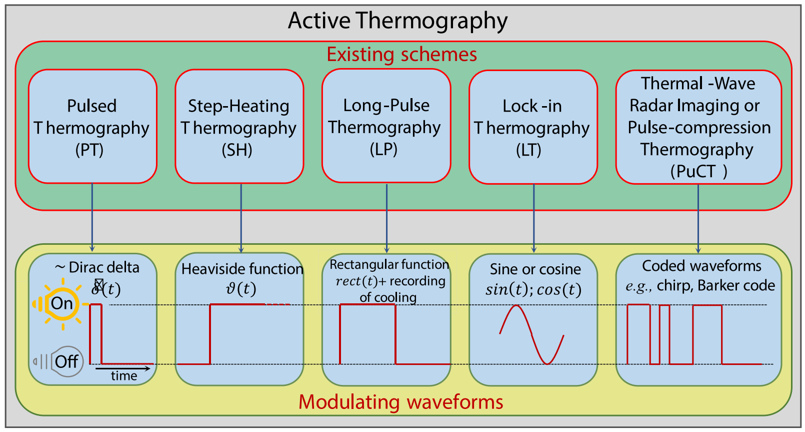

Fig. 1. Taxonomy of the existing AT schemes and related modulating input signals.

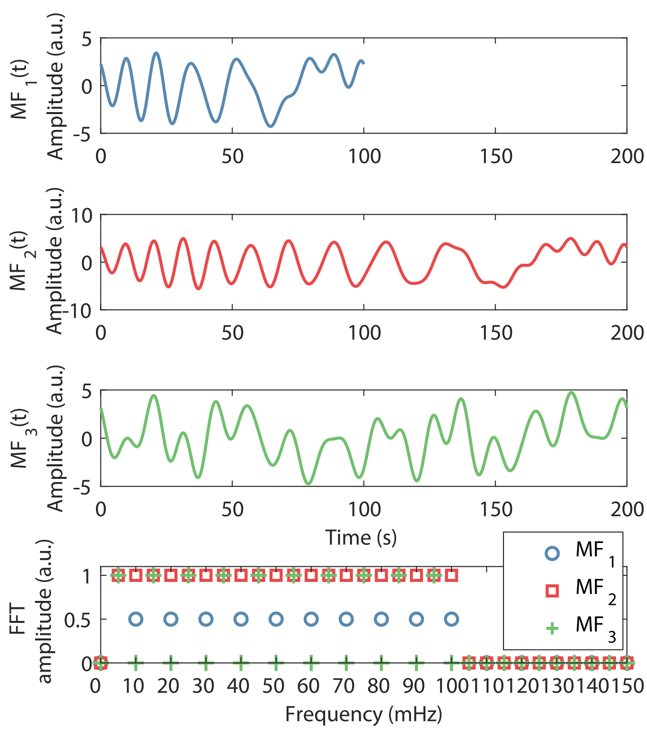

Fig. 2. $MF_1(t)$, $MF_2(t)$, $MF_3(t)$ waveforms, together with their normalized spectra.

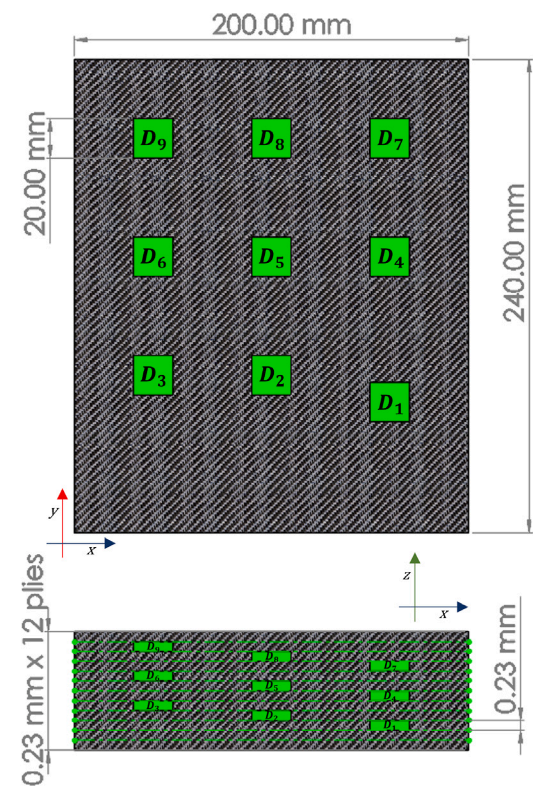

Fig. 3. A quoted sketch of the CFRP sample.

waves"' having different thermal diffusion lengths μ, so that performing *multiple* LI can be time consuming and not suitable in industrial frameworks where a high throughput is sought. Alternative AT schemes are the Step Heating [10], Long Pulse [11], and Pulse-Compression thermography (PuCT) [12–14]. Notwithstanding, the main point is that these alternative schemes aim at combining the pros offered by PT and LI, i.e. exciting a range of depths via a single test and enhancing the maximum achievable SNR corresponding to specific depth' values. The mentioned techniques have all specific pros and cons, which are discussed in detail in the given references.

In this framework, simultaneous multiple-LI analysis exploiting periodic excitations such as square-wave have been proposed starting from the works of Pitarresi [15,16], and introducing recently some further developments in [17–20]. Despite the merits of such schemes, among which the easiness of implementing a square-wave modulation of the heating, it is not possible to choose the number, the order, and the amplitudes of the harmonics, which are indeed determined by the Fourier series expansion of the excitation signal. For instance, with the square-wave modulation, only the fundamental tone and its odd harmonics are excited, and their energy decreases as $\frac{1}{n^2}$, with n being the index of the considered harmonic, so that the number of those useful for LI analysis is limited, as the 5th harmonic has an energy content which is equal to the 4% of the fundamental one, the 7th $\approx 2\%$, etc.

To further improve the multi-LI approach, here we propose for the first time an alternative solution, hereafter referred as *Multi-Frequency Thermography* (MFT), whose pivot is the design and use of an optimized Multi-Frequency (MF) input signal to modulate the emission of a heating system. Although exploiting a periodic excitation, this approach outperforms those based on square or pseudo-square waves, as it relies on the theory of optimal synthesis of low peak-factor multi-tone signals to obtain a single modulating waveform in which both the number of tones and their amplitudes can be chosen with a high flexibility.

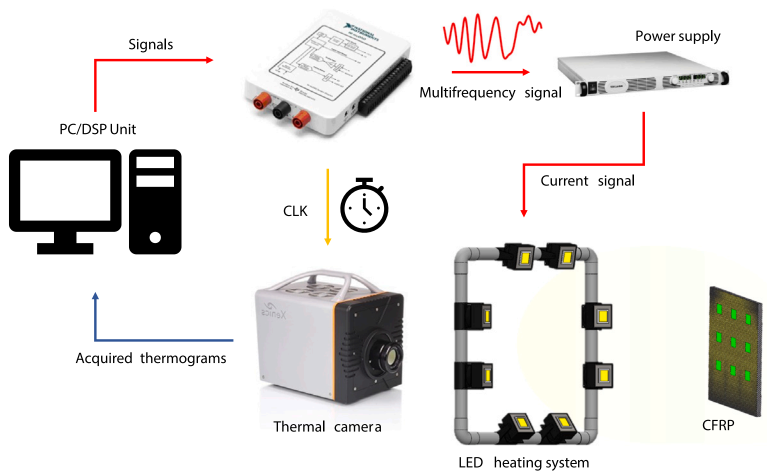

Fig. 4. A sketch of the experimental setup.

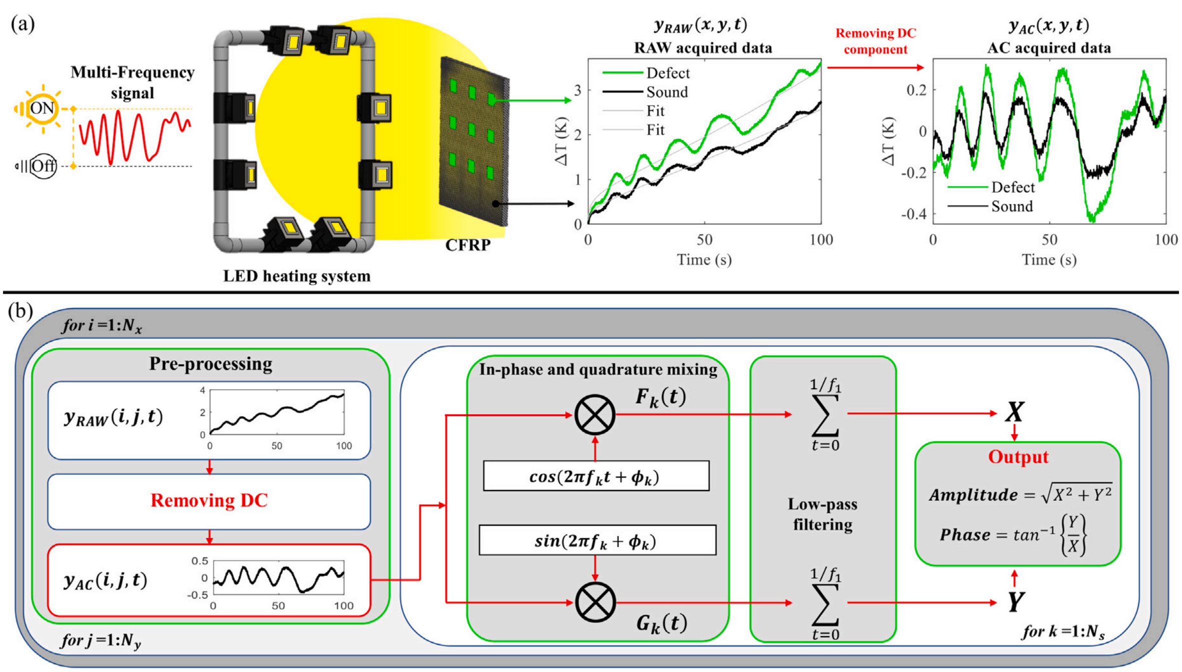

Fig. 5. (a) example of the post-processing step applied to a pixel onto a defect (green) and on a sound one (black); (b) Schematic of the post-processing explaining the whole MF procedure. (For interpretation of the references to color in this figure legend, the reader is referred to the web version of this article.)

More in detail, the MF excitation signals used in this paper are the result of a non-trivial summation of a set of pure tones, whose frequencies are linearly-spaced, all having the same energy and specific initial phase values, as described in [21]. Note that, although the MF waveform can be similar to a frequency modulated chirp signal, their spectra are completely different — the MF has the typical comb-like spectrum of a periodic excitation whereas chirps are characterized by a continuous bandwidth.

The advantages of the proposed solution are that:
(i) the MF contains a desired discrete and finite set of tones, so that a range of specific depths into the sample can be probed via a *single* acquisition, thus emulating the PT and overcoming the limitations of the standard LT;
(ii) the excitation energy is equally distributed on the chosen frequencies, thus improving the state-of-the art of multi-LI based on square- and pseudo-square waves;
(iii) as for the latter approach, the time period of the MF signal remains that of the fundamental tone, despite the number of harmonics selected, so that information are retrieved for all the tones but in the same measurement time of standard LI test at the fundamental frequency, hence making the procedure more efficient.

Note that the introduced MF approach has been successfully exploited in Eddy-Current testing [22,23], so that research made on that field can be highly beneficial for future developments of the MF in AT, and viceversa. Further, it is suitable to be used with all the active thermography methods using a heat source that can be easily analogically modulated, such as LEDs, lasers, induction heaters, and in ultrasound-stimulated thermography, thus being a valid alternative to commonly employed long-pulse thermography.

2. Multi-frequency modulating signal

A generic MF signal $MF(t)$ is here introduced to gain insight on the concept of low-peak factors signals, which result from a combination of some sinusoidal tones exciting a range of frequencies with prescribed

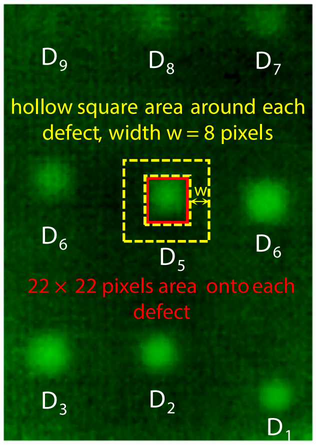

Fig. 6. An example of an acquired thermograms, with marked pixels showing the defect and sound (noise) reference pixels areas for the computation of the SNR.

amplitudes and phases values [21]:

$$MF(t) = \sum_{k=1}^{Ns} s_k cos(2\pi f_k t + \phi_k), \tag{1}$$

with s_k, f_k, and ϕ_k the amplitude, the frequency, and the phase values of the kth sinusoid, respectively, and N_s the number of the tones considered. Assume for simplicity that all f_k are multiple of some fundamental frequency f_0, which can be not present in the summation of Eq. (1), i.e. $f_1 \neq f_0$. The value of f_0 can be small enough so that the constraint on f_k practically does not limit the choice of the tones' frequency. Under this assumption, the $MF(t)$ waveform depends on the values of the phase angles ϕ_k for a given choice of the s_k and f_k values, and it can vary unduly, even if the energy of the signal depends on the s_k values only. Therefore, by considering that in practice the peak power of the excitation is limited, e.g. by the nominal power of a heating/lighting system, it is preferable to choose ϕ_k such that the resulting peak factor of $MF(t)$ is minimized — note that the peak factor of a signal is the ratio between its peak-to-peak and root mean square values. A minimum peak factor guarantees the best SNR among the possible values of the phase angles ϕ_k. It is known from the literature [21] that if the tones are all multiple of a common fundamental frequency, then an expression for the phases ϕ_k exists that minimizes the peak-factor even in presence of tones having different amplitudes s_k. Moreover, if the tones frequencies values are linearly-spaced and have equal amplitudes, and ϕ_k are chosen according to (2), the resulting $MF(t)$ exhibits a *quasi*-constant envelope and the lowest possible peak factor:

$$\phi_k = -\pi \frac{k^2}{N_s}, \text{with } k = 1, 2, \dots, N_s \tag{2}$$

Thus, different thermal waves having a discrete set of thermal diffusion lengths μ are onset within the tested sample by using the so-designed $MF(t)$ as a *single* modulating waveform for the heat source emission.

To gain a visual insight on the $MF(t)$ signals, Fig. 2 shows three examples of $MF(t)$ covering almost the same frequency range but having different discrete spectra.

The characteristics of each of the $MF(t)$ signals, i.e. $MF_1(t)$, $MF_2(t)$, and $MF_3(t)$ are reported in Table 1. $MF_3(t)$ is similar to $MF_2(t)$, but it contains only the odd harmonics of the fundamental tone, so as to highlight the flexibility of the proposed modulation signal. Note that these signals are the ones employed in this work. However, a pre-distortion of these signals was performed in order to consider the nonlinear voltage–irradiance characteristic of the LEDs chips, as detailed in Appendix.

Table 1
Parameters of the employed $MF(t)$ modulating signals.

Signal	Duration (s)	f_1 (mHz)	f_{max} (mHz)	Number of tones
$MF_1(t)$	100	10	100	10
$MF_2(t)$	200	5	100	20
$MF_3(t)$	200	5	95	10

3. Materials and methods

3.1. Benchmark sample and experimental setup

A carbon fiber reinforced polymer (CFRP) with embedded artificial defects at known depths has been selected to show and testing the capability of the proposed MFT approach. The carbon fiber composite laminate sample contained twelve plies of carbon fiber fabric with an areal density of 0.2 $\frac{g}{m^2}$. Its lateral dimensions were 240 mm × 200 mm, with a thickness value of about 2.80 mm. The fibers orientations were 0° and 90° and the matrix was an Epoxy Resin RIM 935. The laminate was made by vacuum assisted resin infusion and it was cured 25 °C and postured at 110 °C for two hours. The artificial delaminations were realized by inserting square pieces of Teflon tape in between specific plies. These had lateral dimensions of 20 mm × 20 mm and thickness equal to 75 μm. Nine artificial defects were inserted into the sample at increasing depths: the shallower, i.e. D_1, was placed under the 2nd ply at a depth 0.46 mm, the deeper, i.e. D_9, under the 10th ply at a depth of about 2.30 mm, see Fig. 3. The thermal diffusivity α of this sample was estimated to be ≈ 0.1 $\frac{mm^2}{s}$ by previous studies [24].

A sketch of the experimental setup used is shown in Fig. 4: the signal generation/acquisition was performed by using a National Instrument myDAQ device, which was connected to a PC and managed through a custom LabVIEW virtual instrument. The myDAQ was used to both feed a TDK Lambda GEN 750 W power supply with the $MF_1(t)$, $MF_2(t)$, and $MF_3(t)$, and generating a clock signal (CLK) to grab thermograms from the IR camera at 10 FPS. A in-house built heating source system consisting of eight LED chips (overall nominal power ~240 W) has been placed at ~300 mm from the tested sample. The thermal camera was a Xenics Onca-MWIR-InSb IR camera arranged in reflection mode and connected to the PC using the Ethernet protocol.

3.2. Multi-frequency lock-in data processing and figures of merit

In the proposed MFT scheme, the post-processing of the acquired thermograms is based on repeating a digital standard Lock-in procedure for each of the tones used in the input signal, so that a family of N_s in-phase $\{X\}$ and quadrature $\{Y\}$ components are obtained.

To gain insight on the procedure, Fig. 5(a) shows the time trend of the temperature/emissivity of two pixels of the acquired thermograms obtained using $MF_1(t)$ as a modulating signal for the LED heating system. In particular, the light green and the black line plot show the increment in temperature ΔT captured by the camera for a pixel onto a defected area and on a sound one, respectively. As expected, a different handling of the ΔT can be appreciated between the two as time elapses. Before performing the MF lock-in, the DC contribution, i.e. the step-heating contribution which is due to the monopolar nature of the heating stimuli, must be removed from the $y_{RAW}(x, y, t)$ [25]. Hence, the so-obtained $y_{AC}(x, y, t)$ contains information on the ΔT that are related to the actual $MF(t)$ employed only. This pre-processing step is referred as "'Removing DC"' in the flowchart in Fig. 5(b), and it is performed by applying a simple non-linear fitting to the $y_{RAW}(x, y, t)$ pixel-wise (N_x and N_y are the amount of pixels captured by the thermal camera). Each of the $y_{AC}(x, y, t)$ is then multiplied by the different tones belonging to the specific $MF(t)$ used, i.e. the one computed as per Eq. (1), and by their quadrature replicas, so as to obtain a number N_s

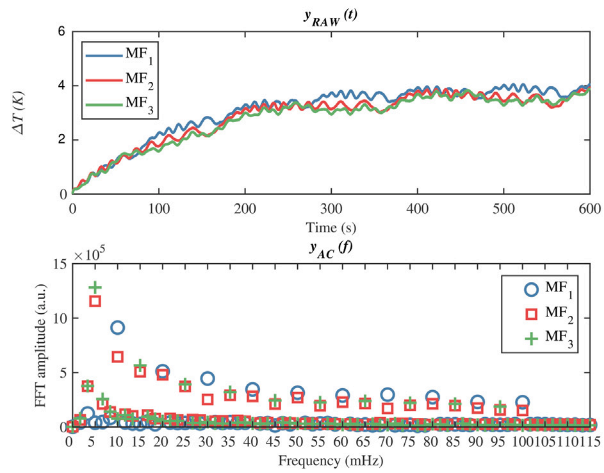

Fig. 7. ΔT values reached by using each of the employed MF signals together with the related spectra obtained after removing the DC component.

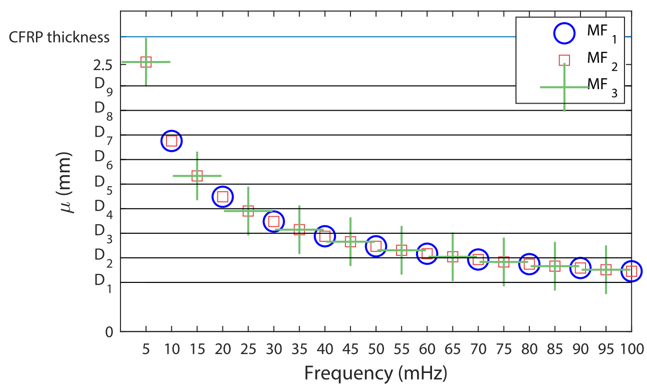

Fig. 8. Values of the theoretical thermal diffusion length for each of MF, together with the depth of each defect. Note that also the whole CFRP tickness value is reported for comparison.

of "'in-phase"' F_k and "'quadrature"' G_k mixing components. Eq. (3) describes the process for a single pixel of the image:

$$
\begin{aligned}
F_k(t) &= y_{AC}(t) * cos(2\pi f_k t + \phi_k),\\
G_k(t) &= y_{AC}(t) * sin(2\pi f_k t + \phi_k),
\end{aligned} \tag{3}
$$

with $k = 1, 2, \ldots, N_s$.

A digital low-pass filter with a cut-off frequency value equal to f_k is then applied over each $F_k(t)$, $G_k(t)$. A quick and reliable way to perform this filtering step is to time-sum each mixing components F_k and G_k along their whole duration $T = \frac{1}{f_1}$ [16], thus obtaining a pair of low-filtered in-phase X and quadrature Y components for each tone. These are then considered as the real and imaginary components of a complex quantity, so that the $Amplitude = \sqrt{X^2+Y^2}$ and $Phase = tan^{-1}\{\frac{Y}{X}\}$ features are obtained accordingly, and they can be used to form images when computed pixel-wise. Although several figures of merit can be established and used to evaluate the capability of the proposed MFT scheme, the value of the achieved SNR at different frequencies is a crucial aspect in any AT test. To shed light on the strategy followed to compute the SNR, Fig. 6 shows an example of a reconstructed thermograms obtained by imaging the quantity $Amplitude$ pixel-wise at a single f_k value, together with two marked areas onto and around a defect. In particular, nine squared areas equal to 22 × 22 pixels have been identified onto each of the defects, see the single red marked area onto D_5 for reference, and these have been used to compute the signal S level. Moreover, nine hollow square areas having a width of 3 pixels have been identified around these, see the yellow-dashed marker. These areas served as references to compute the noise N level. Thus, a series of SNRs values have been obtained for each of the defects, for each considered f_k, for both the $Amplitude$ and $Phase$ features, and for the three $MF(t)$ signals employed, as per (4):

$$
SNR(D_n, f_k) = \frac{|\bar{S}(D_n, f_k) - \bar{N}(D_n, f_k)|}{std[N(D_n, f_k)]}. \tag{4}
$$

where $\bar{S}(D_n, f_k)$ is the mean ($Amplitude$ or $Phase$) value of the pixels within the sound area, $\bar{N}(D_n, f_k)$ is the mean ($Amplitude$ or $Phase$) value of the pixels within the noise area, and std stands for the standard deviation. The obtained results are shown in the next Section.

4. Experimental results

A series of AT tests have been performed using the three MF signals, i.e. $MF_1(t)$, $MF_2(t)$, and $MF_3(t)$, waiting about 1 h in between each acquisition to let the CFRP sample being at the room temperature before starting a new measurement. As a first result, Fig. 7 top subplot, shows the recorded ΔT trends $y_{RAW}(t)$ for a single pixel onto the sample by using six repetitions (periods) of $MF_1(t)$, $MF_2(t)$, and three repetitions $MF_3(t)$. Fig. 7 bottom subplot, depicts corresponding spectra obtained by applying the Fast Fourier Transform to the ΔT trends after the DC component was removed, i.e. the FFT was applied to the $y_{AC}(t)$ signals.

Fig. 7 shows that the spectrum of $MF_1(t)$ captured by the thermal camera covers the bandwidth between 10–100 mHz with discrete steps of 10 mHz, whilst that of $MF_2(t)$ starts from a lower frequency value, i.e. 5 mHz, and covers the bandwidth 5–100 mHz with discrete steps of 5 mHz. On the other hand, the thermal spectrum of $MF_3(t)$ takes almost the same absolute amplitude values of that achieved by $MF_2(t)$, but its amplitude is almost null at even multiples of 5 mHz. Therefore, beside subtle differences at the low frequency values which are ascribable to a non-perfect DC removal, the received spectra are exactly the thermal replicas of that shown in Fig. 2, meaning that the designed MF signals can be faithfully used to excite the desired set of frequencies in AT. Note, however, that a single MF period of excitation has been used in the experiments, whose results are reported hereafter.

It should be also noted that the design of $MF_1(t)$, $MF_2(t)$, and $MF_3(t)$ spectra has been made by considering a trade-off between the actual depth of each of the defects and the overall amount of heat energy to be spread toward the sample, see the ΔT values in Fig. 7, so that a sensitivity at different depths/defects is expected when analyzing the results at each of the values of f_k. For a visual insight, Fig. 8 shows the discrete set of values of the thermal diffusion lengths μ onset into the CFRP sample for each of the employed MF excitation, with μ obtained

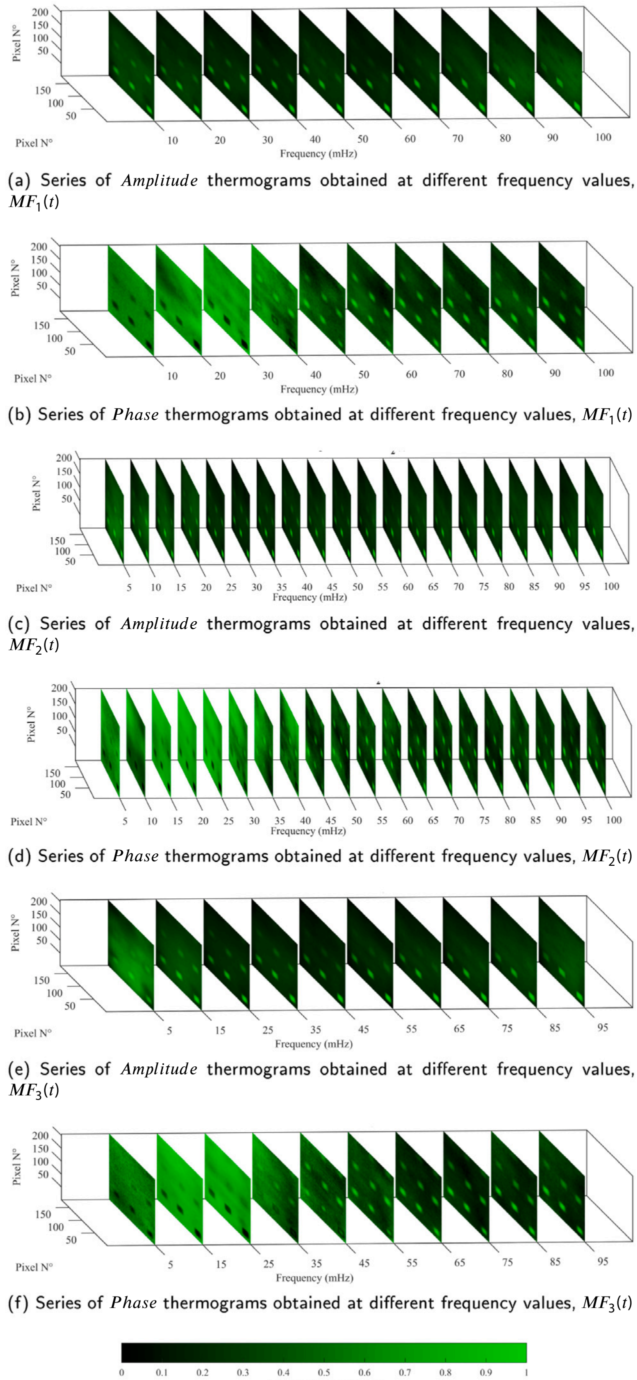

(a) Series of *Amplitude* thermograms obtained at different frequency values, $MF_1(t)$

(b) Series of *Phase* thermograms obtained at different frequency values, $MF_1(t)$

(c) Series of *Amplitude* thermograms obtained at different frequency values, $MF_2(t)$

(d) Series of *Phase* thermograms obtained at different frequency values, $MF_2(t)$

(e) Series of *Amplitude* thermograms obtained at different frequency values, $MF_3(t)$

(f) Series of *Phase* thermograms obtained at different frequency values, $MF_3(t)$

Fig. 9. A series of $x - y$ thermograms at different frequencies for a qualitative analysis.

as per $\mu = \sqrt{\frac{\alpha}{\pi f_k}}$, together with the depths values corresponding to each of the defects buried within the CFRP:

A first qualitative analysis of the depth discrimination capability of the proposed MFT approach can be gathered by imaging the retrieved *Amplitude* and *Phase* at the specific discrete sets of frequencies values belonging to $MF_1(t)$, $MF_2(t)$, and $MF_3(t)$, as depicted in the series of subplots in Fig. 9. The series of thermograms obtained by imaging the *Amplitude* feature demonstrates the good depth discrimination capabilities of the proposed MF approach. For example, Fig. 9(a) shows that the defects buried at a high depth values (D_7, D_8, and D_9 — at the top of each of the thermograms) are imaged at the low frequencies.

Furthermore, their thermal signatures become fainter at higher frequency values, i.e. observing the thermograms from the left to the right, leaving visible the shallower defects only (D_1, D_2, and D_3 — at the bottom of each thermogram) at frequency values toward 100 mHz. The same happens for Fig. 9(c,e), showing also an improved detection of the deeper defects (D_7, D_8, and D_9) with respect to $MF_1(t)$ in Fig. 9(a).

As is known in AT, the *Phase* feature show an improved detection capabilities with respect to the *Amplitude*, especially for the defects at deepest depths, see Fig. 9(b,d,e). Note that D_9 is almost below the detectability level, i.e. SNR close or below the unitary value, in line with other AT tests conducted on the same specimen both using PT and PuCT [24].

To corroborate the qualitative findings, Fig. 10 shows the handling of the $SNR(D_n, f_k)$ for the three MF signals used, both for the

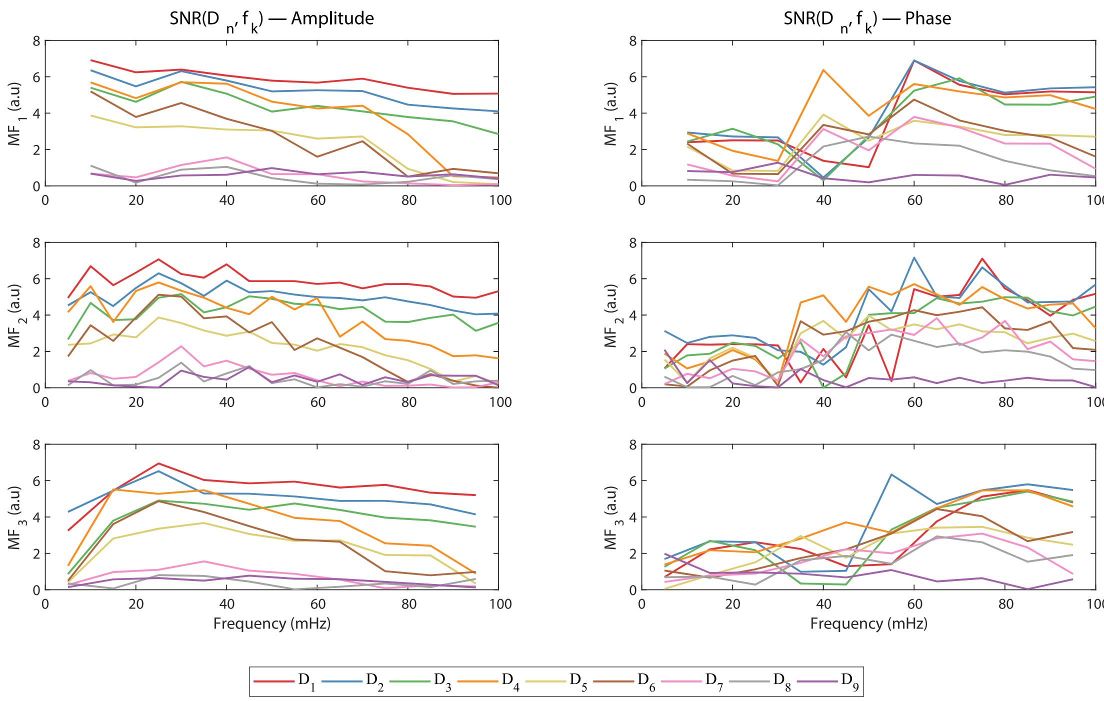

Fig. 10. *Amplitude* and *Phase* SNRs values for the employed signal, for each of the f_k in each of the signal. Note that the values should be discrete, but they are plot as continuous lines for an improved readability.

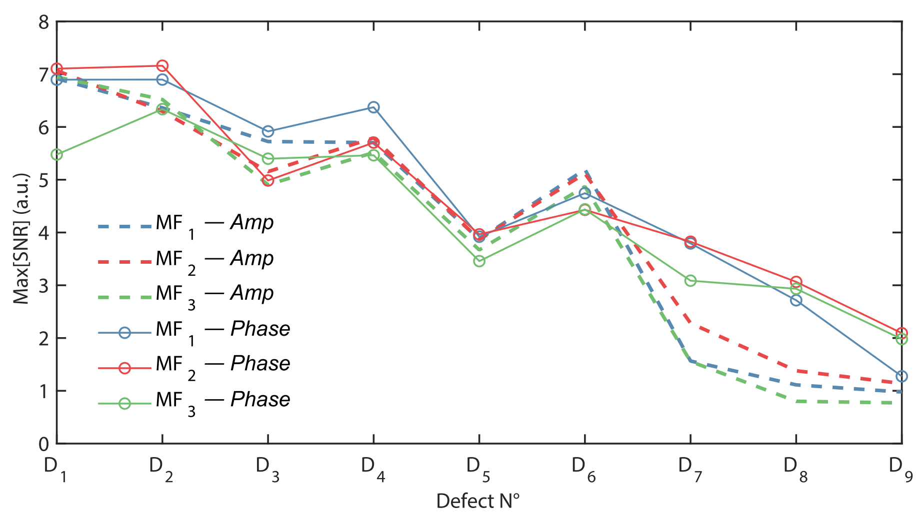

Fig. 11. Maximum *Amplitude* and *Phase* SNRs values obtained using the three MF signals, for each of the defects. Note that the values should be discrete, but they are plotted as continuous lines for an improved readability.

Amplitude and *Phase* features. Although the number of parameters to consider is quite large, a general trend is that the SNR decreases as the depth of the considered defect increases. Furthermore, the SNR values of *Phase* related to deeper defects are slightly higher with respect to their amplitude *Amplitude* counterpart. Also, a relation of the maximum value of the SNR for each investigated defects is taking place — as the depth of the considered defect increases, the higher values of SNR are noticed at increasingly-lower frequency values. Finally, note that the trend of these graphs is in line with what reported in other works such as [11,26,27], where the results of different LI tests operating at various frequencies have been analyzed thoroughly for both CFRP and GFRP samples.

To shed light on the aforementioned behaviors, Fig. 11 depicts the maximum value of the SNR for each of the defects.

It can be noticed that the *Amplitude* and *Phase* features output comparable SNR values up to about D_5, whilst the *Phase* feature shows higher SNRs than the *Amplitude* beyond it.

4.1. Estimation of the defect depths via first-blind frequency approach

In order to estimate the depths of the defects and shows the capability of MFT to discriminate among different depths using a *single* modulating waveform, the first-blind frequency method has been here exploited [28–30]. This entails the computation of the difference between the mean phase angle related to the signal and that of the noise

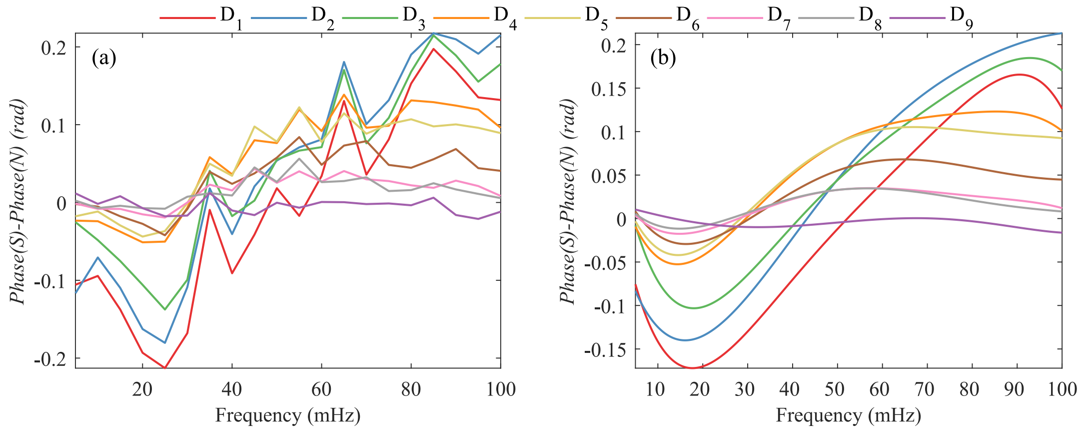

Fig. 12. (a) Phase difference as a function of the frequency values f_k; (b) same as (a), but using a 5th degree fitting polynomial. Different zero-crossing frequency values can be observed for the defects.

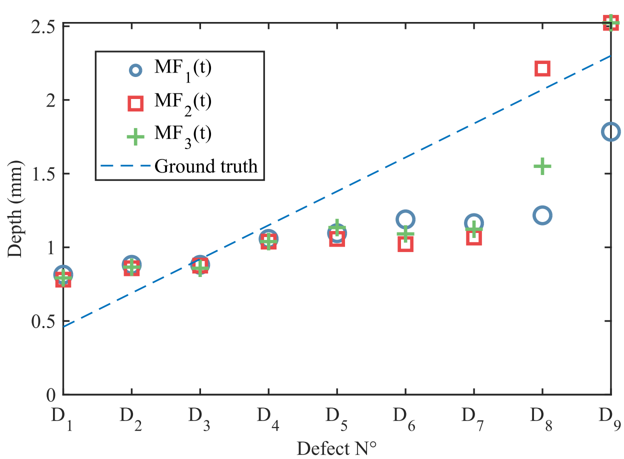

Fig. 13. Estimated defect depths for each of the employed MF signals, together with the ground-truth values.

areas, as established in Section 3.2, and the evaluation of the frequency value f_k^* at which this quantity is equal to zero. This process is shown in (5) for a single defect D_k:

$$f_k^* \, : \, arg\{\bar{S}(f_k)\} - arg\{\bar{N}(f_k)\} = 0 \tag{5}$$

The value of f_k^* that satisfies (5) is stored and used for estimating the defect' depth d_{est} according to $d_{est} = \sqrt{\frac{\alpha}{\pi f_k^*}}$.

The results obtained from $MF_2(t)$ for the nine defects D_k are shown in Fig. 12(a), where it can be noticed that estimating the f_k^* values using the data as is, would yield to a poor frequency resolution $\Delta f = \frac{1}{f_1}$. To circumvent this issue, the data have been fitted using a 5th degree polynomial, resulting in the trends depicted in Fig. 12(b). It can be noticed that the handling of Eq. (5) computed for each of the defects shows a zero-crossing point frequency value f_k^* which is sensitive to the depth, i.e. a higher frequency value for the shallow defects and viceversa. Leveraging the improved frequency resolution, the depths of each of the defects have been estimated according to (5), and reported in Fig. 13.

4.2. Estimation of the defect depths — alternative approach

An alternative method for computing the f_k^* is here proposed to be used in combination with the MFT. This entails the computation of the cumulative of (5):

$$f_k^* \, : \, \sum_{k=1}^{N_k} [\arg\{\bar{S}(f_k)\} - \arg\{\bar{N}(f_k)\}] = 0 \tag{6}$$

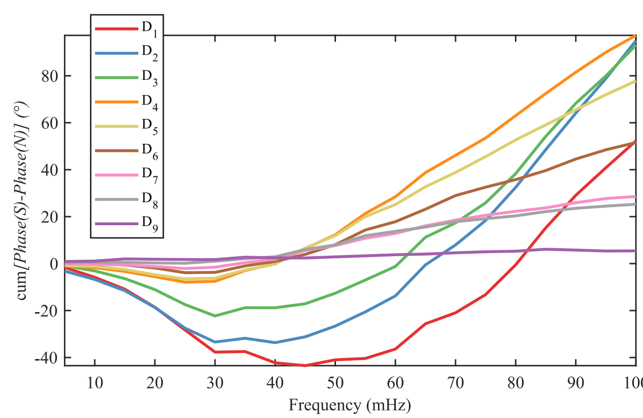

Fig. 14. Cumulative of the phase difference as a function of the frequency values f_k. Different zero-crossing frequency values can be observed for the defects.

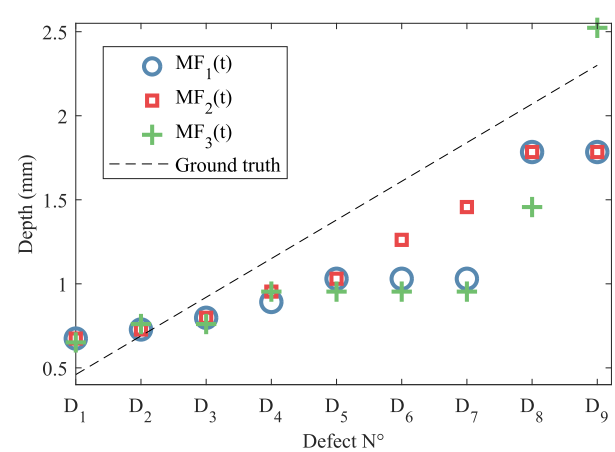

Fig. 15. Estimated defect depths by the cumulative approach for each of the employed MF signals, together with the ground-truth values.

With respect to the standard procedure described in Eq. (5), the proposed algorithm leverages cumulative computation to reduce phase jumps due to noise and avoiding fitting with such a limited number of tones, acting in turn as a low-pass to the phase difference quantity. To get acquainted with the process, Fig. 14 shows the handling of the cumulative obtained for $MF_2(t)$ for the nine defects D_k.

The handling of Eq. (6) computed for each of the defects shows a zero-crossing point frequency value f_k^* which is sensitive to the depth,

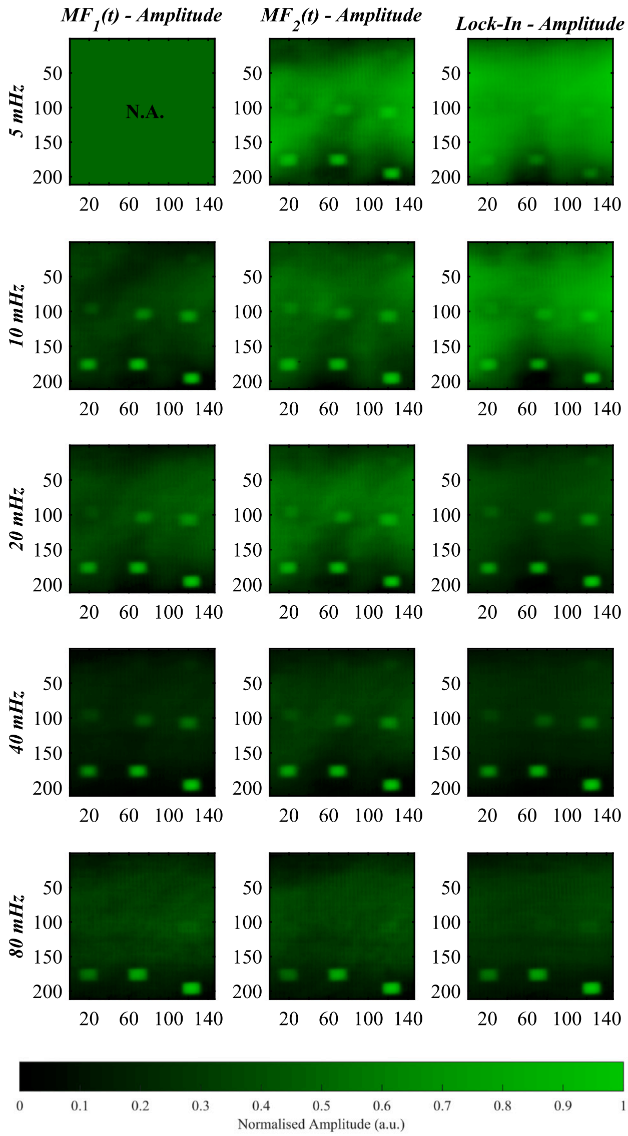

Fig. 16. A series of *Amplitude* thermograms at different frequencies for a qualitative analysis of the MFT and standard LI tests.

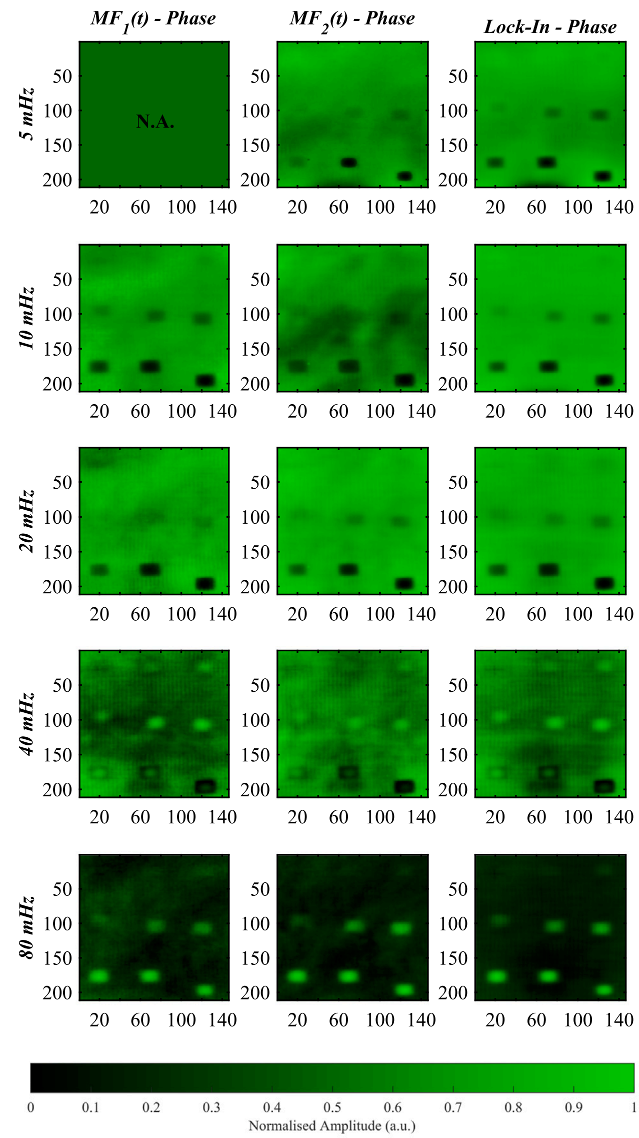

Fig. 17. A series of *Phase* thermograms at different frequencies for a qualitative analysis of the MFT and standard LI tests.

i.e. a higher frequency value for the shallow defects and viceversa. The estimated depth of each of the defects is reported in Fig. 15.

A good agreement is found between the ground-truth and the estimated depths by the proposed MFT methodology. Given the limited number of tones in each of the MF signal, the estimation can be here further improved using e.g. a fitting function as per what shown for the standard procedure, or other method such as the Chirp Z-Transform — these will be handled in future works.

4.3. Comparison of multi-frequency lock-in and standard lock-in thermography

To further corroborate the robustness of the proposed MFT approach, both a quantitative and a qualitative comparison with the standard LI thermography are here reported. Note that the number of cycles of each sinusoidal modulation used in the LI experiments are equivalent to those in each of the $MF(t)$s, and that the same experimental setup and LED power have been used. Fig. 16 shows a series of *Amplitude* thermograms obtained using each $MF_1(t)$ and $MF_2(t)$ at a set of frequency values, together with those achieved with the standard single frequency LI thermography counterpart. Note that $MF_1(t)$ at $f = 5$ mHz is not shown, as this modulating signal is defined starting from 10 mHz. An excellent qualitative agreement is found between the proposed approach and the standard LI one, which is further corroborated by comparing the results achieved using the *Phase* feature, see Fig. 17 — the proposed MFT acts as multiple LI tests, but using a *single* measurement only.

A quantitative comparison reporting the *Phase* SNRs values for each of the defects is shown in Fig. 18, and a good agreement is found here as well. It must be noted that the SNR values achievable using the standard LI can reach higher values by collecting and processing data for a higher and higher number of periods. The same is expected for the MFT, but this will be investigated in future works.

5. Conclusions

An optimized multi-tone signal for modulating the emission of heating systems is here introduced for the first time in active thermography. This is referred as Multi-Frequency Thermography. Both quantitative and qualitative analyses show that this approach can be

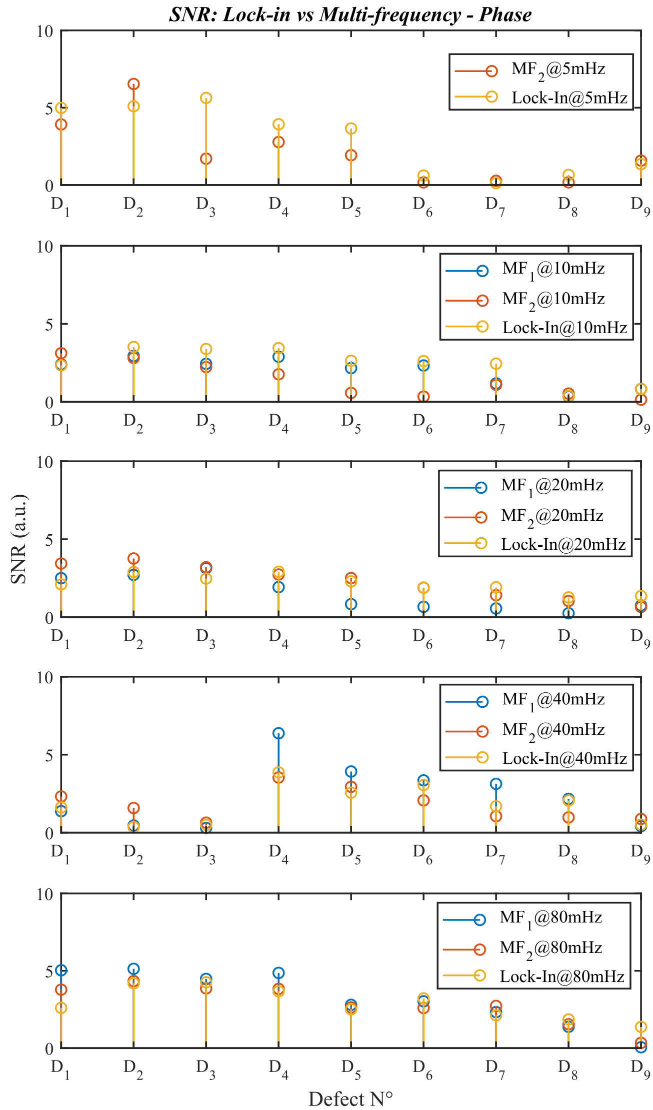

Fig. 18. A comparison of *Phase* SNRs values for a quantitative analysis of the MFT and standard LI tests.

used to replace *multiple* time-consuming standard Lock-in test — a good sensitivity over delaminations buried at different depths is achieved via a *single* test. In addition, the introduced multi-frequency signal shows a constant magnitude of the frequency spectrum for both the even and odd harmonics of a desired fundamental tone, hence overcoming the limitations of the current state-of-the-art. The proposed scheme is suitable to be used with various heating sources, hence representing a valid alternative to PT, LPT, SH, etc.

This first work on the Multi-Frequency Thermography paves the way for future studies on such a technique, which can be used in combination with any other existing active thermography scheme, or can replace them where needed.

CRediT authorship contribution statement

Stefano Laureti: Conceptualization, Data curation, Formal analysis, Investigation, Methodology, Software, Visualization, Writing – original draft, Writing – review & editing, Validation. **Paolo Bison:** Data curation, Formal analysis, Investigation, Validation, Writing – original draft, Writing – review & editing. **Giovanni Ferrarini:** Data curation, Formal analysis, Investigation, Writing – original draft, Writing – review & editing. **Rocco Zito:** Data curation, Formal analysis, Investigation, Software, Writing – original draft, Writing – review & editing. **Marco Ricci:** Conceptualization, Data curation, Formal analysis, Investigation, Methodology, Software, Validation, Writing – original draft, Writing – review & editing.

Declaration of competing interest

The authors declare that they have no known competing financial interests or personal relationships that could have appeared to influence the work reported in this paper.

Data availability

Data will be made available on request.

Acknowledgments

This work was partially supported by the Next Generation EU - Italian NRRP, Mission 4, Component 2, Investment 1.5, call for the creation and strengthening of 'Innovation Ecosystems', building 'Territorial R&D Leaders' (Directorial Decree n. 2021/3277) - project Tech4You - Technologies for climate change adaptation and quality of life improvement, n. ECS0000009. This work reflects only the authors' views and opinions, neither the Ministry for University and Research nor the European Commission can be considered responsible for them.

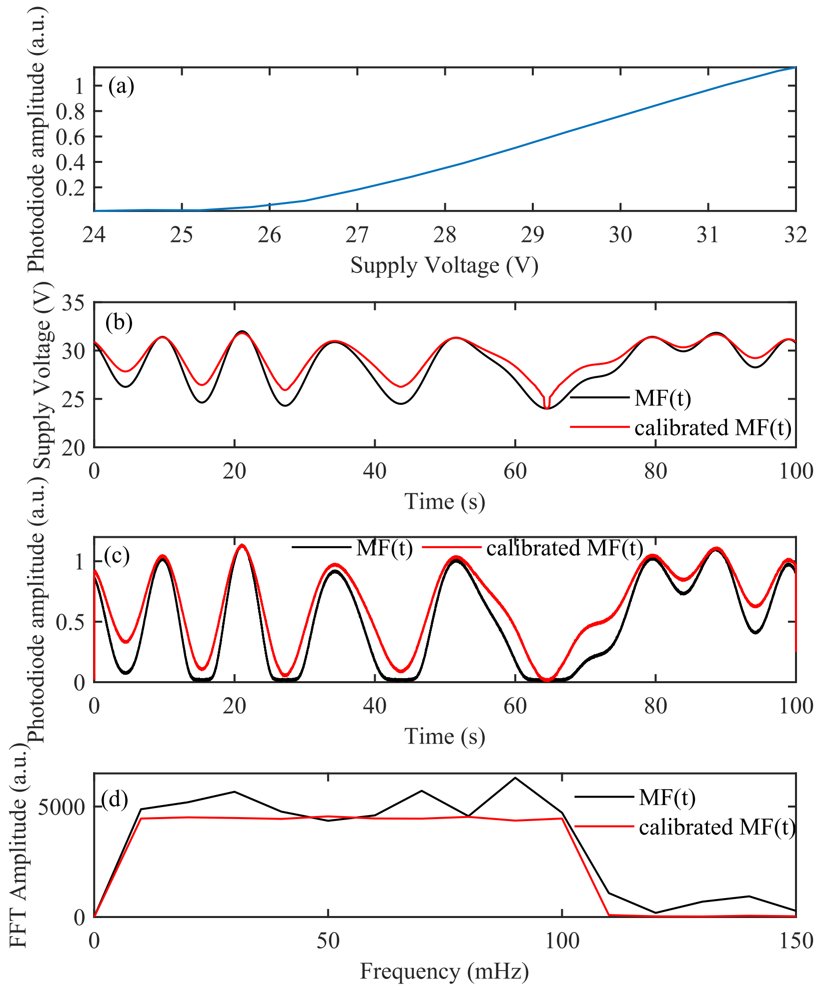

Fig. 19. (a) LED supply voltage and measured amplitude at the photodiode; (b) uncalibrated and calibrated $MF_1(t)$; (c) signal received at the photodiode when the LEDs chips are fed via the uncalibrated and calibrated $MF_1(t)$; (d) Frequency spectrum of the uncalibrated and calibrated $MF_1(t)$.

Appendix. Predistortion of the $MF(t)$ signal

To successfully perform an experiment using a modulating $MF(t)$ to drive the emission of LEDs chips, the nonlinear voltage–current (or voltage–irradiance) characteristic of such sources must be considered. This entails that the $MF(t)$ must be calibrated following the given voltage–current characteristic of the employed LEDs, so as genuine $MF(t)$ can be send over the tested sample without any alteration over the intended spectral content. To this aim, a single characterization of the employed LEDs response over a range of voltages values must be performed. Such range spans from a minimum exploitable voltage, i.e. the value at which the LED chip can be turned on, to a maximum one, i.e. the nominal one. Fig. 19(a) shows the amplitude of the acquired signal from a photodiode ThorLabs PDA10CS-InGaAs placed at about 300 mm from the employed LED systems when the latter is supplied with different voltage values. Note that the minimum and maximum values of the supplied voltage are the same employed to drive the LEDs source to obtain the shown results on the CFRP, i.e. 24–32 V. Fig. 19(b) depicts both a $MF(t)$ signal, i.e. $MF_1(t)$, together with its predistorted counterpart, i.e. the signal calibrated using the V–I handling shown in Fig. 19(a). Although only subtle differences can be appreciated between the time handling of the two signals and on that of the corresponding acquired data by the photodiode, see Fig. 19(c), the FFT of such signals demonstrates that the calibrated $MF(t)$ outputs the intended flat spectrum, a thing that cannot achieved by modulating the LED system with the $MF(t)$ as is, Fig. 19(d). In fact, the use of the uncalibrated signal results in spurious components at frequency higher than 100 mHz, which should not be present, and on an uneven spectral magnitude across 10–100 mHz. Note that the same calibration was used when a single-frequency lock-in was performed.

References

[1] Maldague Xavier, Galmiche François, Ziadi Adel. Advances in pulsed phase thermography. Infrared Phys Technol 2002;43(3–5):175–81.
[2] Wu Jin-Yi, Sfarra Stefano, Yao Yuan. Sparse principal component thermography for subsurface defect detection in composite products. IEEE Trans Ind Inform 2018;14(12):5594–600, Publisher: IEEE.
[3] Laureti S, Sfarra S, Malekmohammadi H, Burrascano Pietro, Hutchins David A, Senni Luca, Silipigni G, Maldague XPV, Ricci Marco. The use of pulse-compression thermography for detecting defects in paintings. Ndt E Int 2018;98:147–54, Publisher: Elsevier.
[4] Gowen AA, Tiwari BK, Cullen PJ, McDonnell K, O'Donnell CP. Applications of thermal imaging in food quality and safety assessment. Trends Food Sci Technol 2010;21(4):190–200, Publisher: Elsevier.
[5] Usamentiaga Ruben, Mokhtari Yacine, Ibarra-Castanedo Clemente, Klein Matthieu, Genest Marc, Maldague Xavier. Automated dynamic inspection using active infrared thermography. IEEE Trans Ind Inf 2018;14(12):5648–57. http://dx.doi.org/10.1109/TII.2018.2836363.
[6] Shepard Steven M, Lhota James R, Rubadeux Bruce A, Wang David, Ahmed Tasdiq. Reconstruction and enhancement of active thermographic image sequences. Opt Eng 2003;42(5):1337–42.
[7] Shepard Steven M. Advances in pulsed thermography. In: Thermosense XXIII, Vol. 4360, SPIE; 2001, p. 511–5.
[8] Breitenstein Otwin, Langenkamp Martin. Lock-in thermography. In: Basics and use for functional diagnostics of electronics components. 2003.
[9] Lei Lei, Ferrarini Giovanni, Bortolin Alessandro, Cadelano Gianluca, Bison Paolo, Maldague Xavier. Thermography is cool: Defect detection using liquid nitrogen as a stimulus. NDT E Int 2019;102:137–43.

[10] Balageas Daniel L, Roche Jean-Michel, Leroy François-Henri, Liu Wei-Min, Gorbach Alexander M. The thermographic signal reconstruction method: A powerful tool for the enhancement of transient thermographic images. Biocybern Biomed Eng 2015;35(1):1–9.
[11] Almond Darryl P, Pickering Simon G. An analytical study of the pulsed thermography defect detection limit. J Appl Phys 2012;111(9).
[12] Yi Qiuji, Malekmohammadi Hamed, Tian Gui Yun, Laureti Stefano, Ricci Marco. Quantitative evaluation of crack depths on thin aluminum plate using eddy current pulse-compression thermography. IEEE Trans Ind Inf 2019;16(6):3963–73.
[13] Tabatabaei Nima, Mandelis Andreas. Thermal-wave radar: A novel subsurface imaging modality with extended depth-resolution dynamic range. Rev Sci Instrum 2009;80(3):034902.
[14] Wang Fei, Wang Yonghui, Liu Junyan, Wang Yang. The feature recognition of cfrp subsurface defects using low-energy chirp-pulsed radar thermography. IEEE Trans Ind Inf 2019;16(8):5160–8.
[15] Pitarresi G. Thermal nde of thick grp panels by means of a pulse modulated lock-in thermography technique. In: EPJ web of conferences. Vol. 6, EDP Sciences; 2010, p. 38014.
[16] Pitarresi G. Lock-in signal post-processing techniques in infra-red thermography for materials structural evaluation. Exp Mech 2015;55:667–80.
[17] Kopera Bernd AF, Retsch Markus. Multiplexed lock-in thermography. Rev Sci Instrum 2021;92(1).
[18] D'Accardi Ester, Palumbo Davide, Galietti Umberto. A comparison among different ways to investigate composite materials with lock-in thermography: the multi-frequency approach. Materials 2021;14(10):2525.
[19] Zhu Pengfei, Wu Dan, Wang Yifan, Miao Zhifei. Defect detectability based on square wave lock-in thermography. Appl Opt 2022;61(21):6134–43.
[20] Matarrese Tiziana, Palumbo Davide, Galietti Umberto. Comparison in the transient regime of four lock-in thermography algorithms by means of synthetic and experimental data on cfrp. NDT E Int 2023;139:102925.
[21] Schroeder Manfred. Synthesis of low-peak-factor signals and binary sequences with low autocorrelation corresp. IEEE Trans Inf Theory 1970;16(1):85–9.
[22] Betta Giovanni, Ferrigno Luigi, Laracca Marco, Burrascano Pietro, Ricci Marco, Silipigni Giuseppe. An experimental comparison of multi-frequency and chirp excitations for eddy current testing on thin defects. Measurement 2015;63:207–20.
[23] Ricci Marco, Silipigni Giuseppe, Ferrigno Luigi, Laracca Marco, Adewale Ibukun D, Tian Gui Yun. Evaluation of the lift-off robustness of eddy current imaging techniques. NDT E Int 2017;85:43–52.
[24] Silipigni Giuseppe, Burrascano Pietro, Hutchins David A, Laureti Stefano, Petrucci Roberto, Senni Luca, Torre Luigi, Ricci Marco. Optimization of the pulse-compression technique applied to the infrared thermography nondestructive evaluation. NDT E Int 2017;87:100–10.
[25] Hedayatrasa Saeid, Poelman Gaétan, Segers Joost, Paepegem Wim Van, Kersemans Mathias. Phase inversion in (vibro-) thermal wave imaging of materials: Extracting the ac component and filtering nonlinearity. Struct Control Health Monit 2022;29(4):e2906.
[26] Chatterjee Krishnendu, Tuli Suneet, Pickering SimonG, Almond Darryl P. A comparison of the pulsed, lock-in and frequency modulated thermography nondestructive evaluation techniques. Ndt E Int 2011;44(7):655–67.
[27] Pickering Simon, Almond Darryl. Matched excitation energy comparison of the pulse and lock-in thermography nde techniques. Ndt E Int 2008;41(7):501–9.
[28] Ibarra-Castanedo Clemente, Maldague Xavier P. Defect depth retrieval from pulsed phase thermographic data on plexiglas and aluminum samples. In: Thermosense XXVI, Vol. 5405, SPIE; 2004, p. 348–56.
[29] Almond Darryl P, Patel Pravin. Photothermal science and techniques, Vol. 10, Springer Science & Business Media; 1996.
[30] Carslaw Horatio Scott, Jaeger John Conrad, Feshbach Herman. Conduction of heat in solids. Phys Today 1962;15(11):74–6.